Purdue University
Purdue e-Pubs

PRISM: NNSA Center for Prediction of Reliability, Integrity and Survivability of Microsystems

Birck Nanotechnology Center

4-1-2009

Compact Model Of Squeeze-Film Damping Based On Rarefied Flow Simulations

Xiaohui Guo
Purdue University - Main Campus, xguo@purdue.edu

Alina Alexeenko
Purdue University - Main Campus, alexeenk@purdue.edu

Follow this and additional works at: http://docs.lib.purdue.edu/prism

Part of the Nanoscience and Nanotechnology Commons

Guo, Xiaohui and Alexeenko, Alina, "Compact Model Of Squeeze-Film Damping Based On Rarefied Flow Simulations" (2009). *PRISM: NNSA Center for Prediction of Reliability, Integrity and Survivability of Microsystems.* Paper 15.
http://docs.lib.purdue.edu/prism/15

This document has been made available through Purdue e-Pubs, a service of the Purdue University Libraries. Please contact epubs@purdue.edu for additional information.

IOP PUBLISHING JOURNAL OF MICROMECHANICS AND MICROENGINEERING

J. Micromech. Microeng. **19** (2009) 045026 (7pp) doi:10.1088/0960-1317/19/4/045026

Compact model of squeeze-film damping based on rarefied flow simulations

Xiaohui Guo and Alina Alexeenko

School of Aeronautics and Astronautics, Purdue University, West Lafayette, IN 47907, USA

E-mail: alexeenk@ecn.purdue.edu

Received 10 November 2008, in final form 27 February 2009
Published 26 March 2009
Online at stacks.iop.org/JMM/19/045026

Abstract
A new compact model of squeeze-film damping is developed based on the numerical solution of the Boltzmann kinetic equation. It provides a simple expression for the damping coefficient and the quality factor valid through the slip, transitional and free-molecular regimes. In this work, we have applied statistical analysis to the current model using the chi-squared test. The damping predictions are compared with both Reynolds equation-based models and experimental data. At high Knudsen numbers, the structural damping dominates the gas squeeze-film damping. When the structural damping is subtracted from the measured total damping force, good agreement is found between the model predictions and the experimental data.

Nomenclature

A, B, c, d, e	damping force coefficients
C_1, C_2	quality factor coefficients
b	cantilever width, m
c_f	damping coefficient, N s m^{-1}
E	Young's modulus, GPa
F, F_0	damping force, N
f	frequency, Hz
f, f_0	velocity distribution function
g	gap height, m
j	complex unit
Kn	Knudsen number
L	cantilever length, m
n	molecular number density, m^{-3}
Pr	Prandtl number
$p, P_A, \mathbf{p}_{ij}$	pressure/pressure tensor, Torr
Q	quality factor
Q_{pr}	relative flow rate coefficient
q	complex frequency variable
R	specific gas constant, J (K kg)$^{-1}$
Re	Reynolds number
r^2	Pearson r^2
t	cantilever thickness, m
u, v	molecular velocity, m s^{-1}
u', v'	thermal velocity, m s^{-1}
u_0, v_0	bulk velocity, m s^{-1}
v_s	cantilever speed, m s^{-1}
x_1, x_2	independent variables

Greek symbols

β_0, β_1	linear regression coefficients
χ^2	chi-squared test (distribution)
δ_{ij}	Kronecker delta
γ	ratio of specific heats (=1.4)
γ_n	vibration coefficients
$\mathbf{\Lambda}_{ij}$	coefficient matrix in ESBGK
λ	molecular mean-free-path, m
μ	viscosity, kg (m s)$^{-1}$
ν	collision frequency, s^{-1}
ρ, ρ_s	density, kg m^{-3}
σ	tangential momentum accommodation coefficient (TMAC)
ω	angular frequency, rad s^{-1}
ζ_n	damping ratio

Acronyms

RF	radio frequency
MEMS	micro-electro-mechanical systems
SFD	squeeze-film damping
NSSJ	Navier–Stokes slip jump
DSMC	direct simulation Monte Carlo
BGK	Bhatnagar–Gross–Krook
ES-BGK	ellipsoidal statistical BGK
CADP	cantilever array discovery platform

 © 2009 IOP Publishing Ltd Printed in the UK

1. Introduction

Design of resonant sensors [1–6], RF MEMS switches [7] and scanning probes [8] requires predictions of gas forces on moving micron-sized structures. In many such applications, there are long, thin gaps with surfaces in relative motion. Due to the large surface-to-volume ratio in micro-devices, gas damping plays an important role in determining the dynamic motion. In particular, the dominant damping source in planar microstructures is the squeeze-film damping (SFD) [9]. As is explained by its name, squeeze-film damping is the force generated when the fluid is pulled in or pushed out of a thin gap.

The SFD phenomena often involve non-continuum fluid flow effects due to the small gap size. This becomes even more significant when a microsystem operates at low pressures. The non-dimensional parameter used for quantifying the non-continuum fluid behavior is the Knudsen number (Kn), which is defined as the ratio of gas molecular mean-free-path to the characteristic length of the system [10]. There are a number of published gas damping theories and models, which are valid for certain geometries and Knudsen number ranges [12, 13].

In the present work, we propose a new compact model of squeeze-film damping based on the numerical solution of the Boltzmann kinetic equation. The model gives a simple expression for the damping coefficient and the quality factor valid for Knudsen numbers ranging from 0.05 to 100 and is applicable to planar geometries.

In the following section, we review previous gas damping models based on the Reynolds equation. Next, we describe the numerical simulations based on the Boltzmann kinetic equation. The damping forces predicted by the simulations are then compared with both analytical results and experimental data. Finally, we present statistical analysis of the compact model and discuss the effects of structural damping at high Knudsen numbers.

2. Gas damping models

For a micro-oscillating cantilever system, the damping ratio, ζ, and the quality factor, Q, of its nth vibration mode can be defined as follows [11]:

$$\zeta_n = \frac{c_f}{2\rho_s b t \omega_n} = \frac{1}{2Q_n} \tag{1}$$

$$c_f = \frac{F}{v_s L} \tag{2}$$

$$\omega_n = \gamma_n^2 \sqrt{\frac{EI}{\rho_s b t L^4}}, \tag{3}$$

where b is the beam width, t is the thickness, L is the length, E and I ($= bt^3/12$) refer to the Young's modulus and area moment of inertia of the cantilever respectively and ρ_s is the mass density of structure. For a cantilever beam, the nth natural resonant frequency of vibration ω_n is given by its characteristic function where γ_n are 1.8751, 4.9641 and 7.8548 for the first three modes of fixed-free cantilevers, and are 4.7300, 7.8532 and 10.9956 for the first three modes of fixed-fixed (clamped) beams. As shown in equation (1), the quality factor, Q_n, increases proportionally with the resonant frequency, ω_n, for the same damping force c_f.

The Reynolds equation has been widely used to describe gas motion of the squeeze-film damping problem. In general, it assumes rigid plate, small gas size, small structural displacement and small pressure variation. For one-dimensional damping under these assumptions, the Reynolds equation reduces to

$$\frac{\partial(\rho g)}{\partial t} = \nabla \cdot \left(\frac{\rho g^3}{12\mu} Q_{pr} \nabla p \right), \tag{4}$$

where g is the gap height, ρ is the gas density, p is the pressure, μ is the viscosity and Q_{pr} is the relative flow rate coefficient to be specified.

2.1. Unsteady Reynolds equation with inertia effects

A model developed by Veijola [12] gives a frequency-dependent expression for Q_{pr} assuming trivial boundary conditions:

$$Q_{pr} = \frac{12\mu}{\mathrm{j}\omega\rho g^2 (qg)} \left[\frac{(qg) - (2 - Kn^{(g)}(qg)^2)\tanh(qg/2)}{1 + Kn^{(g)}(qg)\tanh(qg/2)} \right] \tag{5}$$

$$Kn^{(g)} = \frac{\lambda}{g} \tag{6}$$

$$qg = \sqrt{\mathrm{j}\frac{\rho}{\mu}\omega} = \frac{1}{g}\sqrt{\mathrm{j}\frac{\rho g^2}{\mu}\omega} = \frac{1}{g}\sqrt{\mathrm{j}Re}, \tag{7}$$

where $Kn^{(g)}$ is the Knudsen number based on the gap height, Re is the modified Reynolds number, q is a complex frequency variable and j is the complex unit.

2.2. Modified Reynolds equation

The correlation developed by Gallis and Torczynski [13] is based on the Reynolds equation with Navier–Stokes slip jump (NSSJ) boundary for $Kn < 0.1$ and the results of the direct simulation Monte Carlo (DSMC) method for $Kn < 1.0$. It takes advantages of the simplicity of the Reynolds equation and includes molecular effects. One biggest advantage for this model is the removal of trivial boundary conditions, which significantly improves the accuracy of damping predictions based on the Reynolds equation when the gap size is non-negligible compared to the beam width, e.g. $b/g < 10$. Note that in both the NSSJ and DSMC simulations, the specular-reflection boundary condition was applied due to the cantilever array geometry considered in [13]. As a result, the domain size becomes critical when considering higher Kn numbers.

3. Numerical simulations

3.1. Governing equation and boundary conditions

Assuming that the length of the microcantilever is much larger than the width and thickness, and that the vibration amplitude is much smaller than the gap height, the SFD problem can

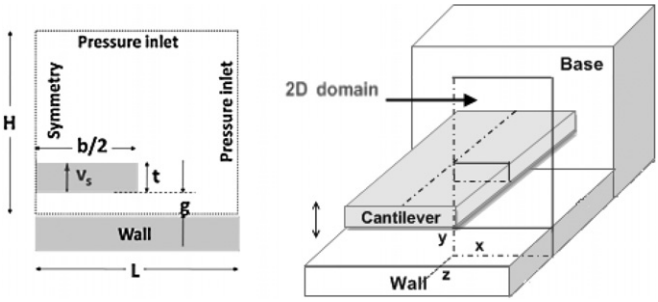

Figure 1. Schematic of SFD for microcantilevers.

be solved through two-dimensional simulations. The quasi-steady Boltzmann kinetic model for the velocity distribution function f can be given as [14]

$$u\frac{\partial f}{\partial x} + v\frac{\partial f}{\partial y} = \nu(f_0 - f), \tag{8}$$

where u and v are the gas molecular velocities in the x and y directions, respectively, ν is the collision frequency and f_0 is the equilibrium distribution function. The ellipsoidal statistical Bhatnagar–Gross–Krook (ES-BGK) model for the collision relaxation uses f_0 as [15]

$$f_0 = f_{ES} = \frac{n}{\sqrt{(2\pi)^3 \det(\boldsymbol{\Lambda}_{ij})}} \exp\left(-\frac{u'v'}{2\boldsymbol{\Lambda}_{ij}^{-1}}\right) \tag{9}$$

$$\boldsymbol{\Lambda}_{ij} = RT\delta_{ij} + \left(1 - \frac{1}{Pr}\right)\frac{\boldsymbol{p}_{ij}}{\rho} \tag{10}$$

$$u' = u - u_0, \qquad v' = v - v_0 \tag{11}$$

where n is the gas number density, u' and v' are the molecular thermal velocities, u_0 and v_0 are the bulk velocities, R is the specific gas constant, $\boldsymbol{p}_{ij}$ is the pressure tensor, ρ is the density, Pr is the Prandtl number and δ_{ij} is the Kronecker delta.

The SFD problem is solved numerically in the computational domain shown in figure 1. The symmetric boundary condition is applied on the left side of the computational domain. The pressure inlet conditions are applied at the top and right boundaries. The diffuse-reflection boundary condition is applied at the base and the side wall of the microcantilever. The diffuse-reflection boundary condition with a relative bulk velocity is used on the top and bottom surfaces of the microcantilever. An accommodation coefficient of 1.0 has been used in all cases. Geometry and flow conditions are summarized in table 1.

3.2. Discretization and schemes

The governing equation (8) is solved numerically using a Fortran 90 code developed by the authors. The solver employs the finite volume method in the physical coordinate space and the discrete-ordinate method in the velocity space. A second-order quadrant-splitting scheme is applied in the physical space and a 16th-order Gauss–Hermite quadrature is applied to the velocity magnitude [16]. Validation of the numerical approach has been published in an earlier work by the authors in [17]. Based on the mesh convergence study, we choose a non-uniform grid with the minimum grid resolution less than 0.5 μm for the reported results. The domain size has stronger influence for low pressures than for atmospheric pressures because of the changes of molecular mean-free-path. As shown in figure 2, the pressure differences for various domain sizes are less than 0.3% and 3.0% for cases with ambient pressures being 760 Torr (1.0 atm) and 0.76 Torr (0.001 atm), respectively.

Table 1. Microcantilever geometry and flow conditions.

Property	Symbol	Nominal value
Cantilever length	L	500.0×10^{-6} m
Cantilever width	b	18.0×10^{-6} m
Cantilever thickness	t	2.25×10^{-6} m
Gap height	g	$(1.0, 1.2, 1.4, 1.6, 1.8) \times 10^{-6}$ m
Velocity	v_s	<10 m s^{-1}
Frequency	f	10^4–10^6 Hz
Amplitude	A	$\sim 10^{-9}$ m
Gas	(N_2, O_2)	Air
Viscosity	μ	1.78×10^{-5} Pa s
Temperature	T	295 K
Pressure	P_A	10^{-3}–10^2 Torr
TMAC	σ	1.0

Table 2. Microcantilever geometry and flow conditions [13].

Property	Symbol, unit	Nominal value
Cantilever width	b	20.0×10^{-6} m
Cantilever thickness	t	2.0×10^{-6} m
Gap height	g	2.0×10^{-6} m
Velocity	v_s	<10 m s^{-1}
Gas	(N_2, O_2)	Air
Viscosity	μ	1.753×10^{-5} Pa s
Temperature	T	295 K
Pressure	P_A	76.0 Torr
TMAC	σ	1.0

4. Comparison with previous models

In the quasi-steady two-dimensional ES-BGK simulations, the damping coefficient c_f is obtained by integrating the computed normal pressure component P_{yy} along the width of the cantilever cross section and normalizing by the velocity v_s. In general, c_f is independent of the cantilever moving velocity as long as v_s is small compared to the gas mean thermal velocity.

4.1. Pressure distribution

First, the pressure distributions from simulations of Gallis–Torczynski [13] has been compared for $Kn = 0.1$. Detailed microcantilever geometry and gas flow conditions are listed in table 2. As shown in figure 4, the ES-BGK solution agrees well with NSSJ and DSMC results. Also shown in figure 3 are the solutions of the Reynolds equations with trivial boundary conditions [12]. It is important to note that for a moderate aspect ratio, i.e. $b/g = 10.0$, the trivial boundary condition results in significant under-prediction of the damping force. In other words, when the gap size is large compared to the

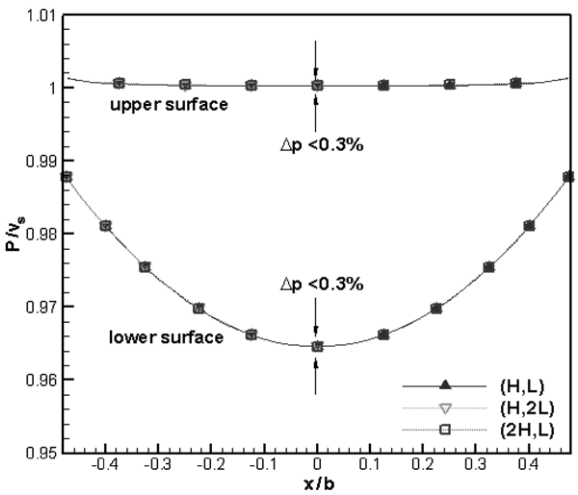

(*a*) P_A = 760 Torr, $Kn^{(g)}$ = 0.05

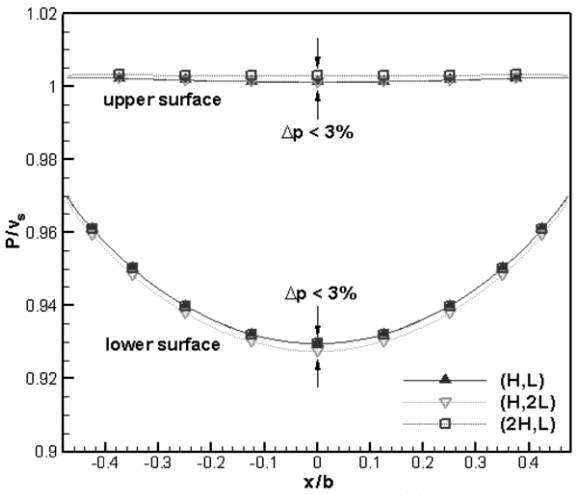

(*b*) P_A = 0.76 Torr, $Kn^{(g)}$ = 50.0

Figure 2. Pressure distributions along top and bottom surfaces.

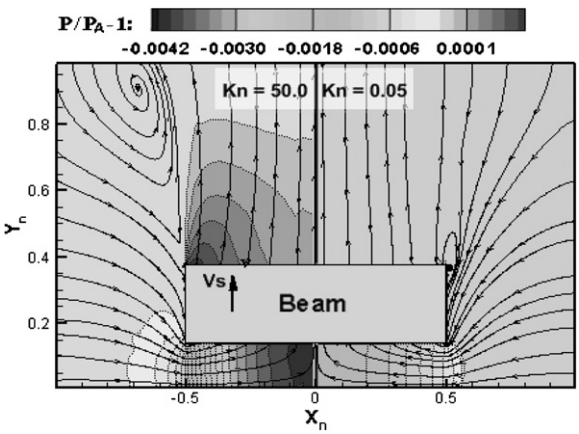

Figure 3. Pressure field and streamlines under different rarefaction conditions. $Kn = 50.0$ (left) and 0.05 (right).

cantilever width, pressure jumps at both edges must be taken into account.

Figure 5 shows that the difference between the total pressure, P, and its component in the y direction normal to

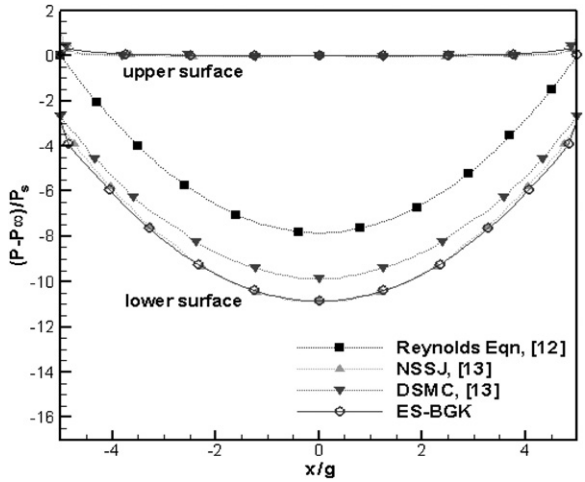

Figure 4. Comparisons of pressure distributions [12, 13].

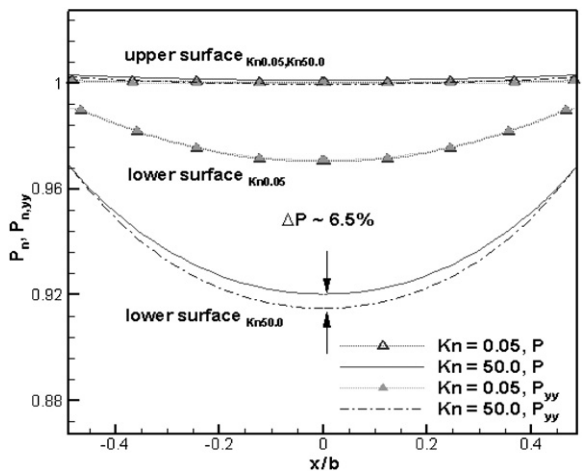

Figure 5. Non-equilibrium effects on pressures at different Kn.

Table 3. Microcantilever natural frequencies.

Property	Symbol	Value
Mode 1	f_1	12.0 kHz
Mode 2	f_2	84.4 kHz
Mode 3	f_3	211.4 kHz

the cantilever upper and lower surfaces, P_{yy}, can be as much as 6.5% at $Kn = 50$ due to non-equilibrium effects. In other words, in quality factor calculations, the results obtained by using the total pressures P instead of P_{yy} may lead to an over-prediction of damping force at high Knudsen numbers.

4.2. Quality factor

The geometry of Sandia CADP-chip 2 (cantilever array discovery platform) [18] has been considered in the ES-BGK simulation, and the geometric properties and conditions can be found in table 1. The theoretical frequencies for the first three vibration modes according to equation (3) are listed in table 3.

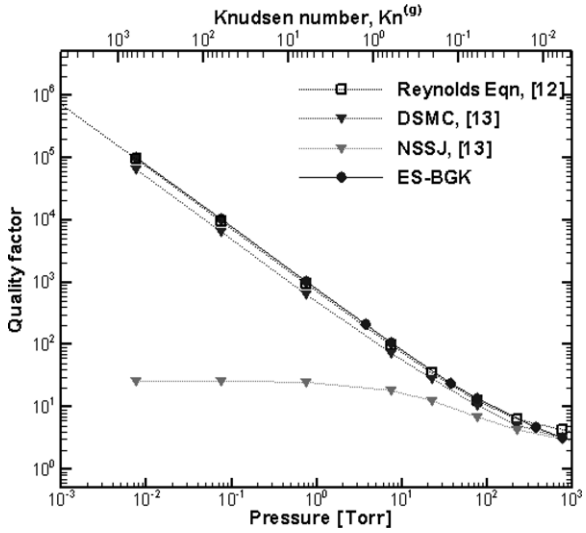

Figure 6. Comparisons of quality factors for mode 3 [12, 13].

As shown in figure 6, good agreement has been found for comparisons between ES-BGK calculations and Reynolds equation-based Veijola model and NSSJ–DSMC-based Gallis–Torczynski correlations. However, the match may not lead to a conclusion that the Reynolds equation reflects the real physics at high Knudsen cases.

The Reynolds equation-based model tends to over-predict quality factors at low pressures in general. However, trivial boundary effects tend to exaggerate and under-predict quality factors at low pressures. Therefore, the overall prediction by Veijola's model appears to give a quality factor close to its real value but for non-physical reasons. In comparison, the NSSJ–DSMC correlation with non-trivial boundary conditions works well for $Kn < 1.0$ and slightly under-predicts the quality factor at high Kn. As the quality factor grows almost linearly with decreasing pressure for $Kn > 1.0$, one can expect that a linear extension of the original correlation from low to high Kn should give close predictions of quality factors. However, at low pressures, the wall boundary conditions may impose artificial effects for the flow field due to large molecular mean-free-path.

5. ES-BGK-based model

5.1. Compact model based on rarefied flow simulations

A closed-form SFD correlation is developed based on fifty quasi-steady two-dimensional ES-BGK simulations for gap-based Knudsen numbers, $Kn^{(g)}$, varying from 0.05 to 50, microcantilever aspect ratios, b/t, varying from 2.0 to 80.0 and ratios of the beam width to the gap height, b/g, varying from 10.0 to 18.0. Unlike free vibrations, the non-dimensional parameter b/t is not as important as Kn and b/g for SFD problems. As shown in figure 7, the damping coefficient, c_f, is less sensitive to the gap size at lower pressures than it is at higher pressures.

The choice of the mathematical format for the new correlation takes into account Veijola's model for low

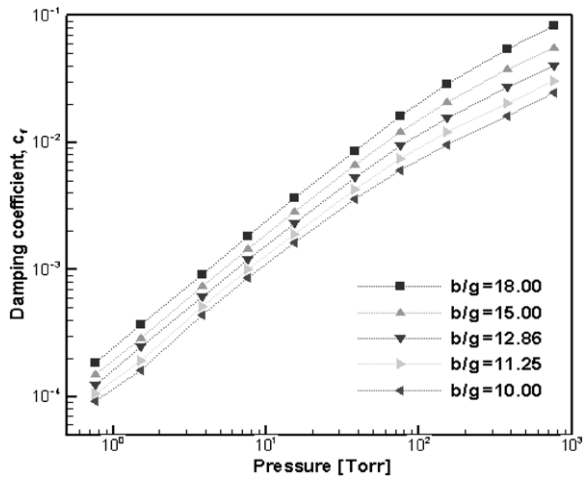

Figure 7. Damping coefficient c_f simulations using ES-BGK.

frequency damping modes and the Q_{pr} correlation at low pressures:

$$c_f = \frac{F_0}{v_s L} = \frac{(b/g)^3 t}{Q_{pr}} \tag{12}$$

$$Q_{pr} = 1 + 9.638 \cdot [Kn^{(g)}]^{1.159} \tag{13}$$

$$Kn^{(g)} = \frac{b}{g} \cdot Kn^{(b)}. \tag{14}$$

Let $x_1 = b/g$ and $x_2 = Kn^{(b)} = x_1 \cdot Kn^{(g)}$, and substitute equations (13) and (14) into (12); then the damping force can be rearranged in the following form:

$$c_f(x_1, x_2) = \frac{F_0}{v_s L} = \frac{A x_1^c}{1 + B x_1^d x_2^e} \cdot t. \tag{15}$$

In the proposed new model, the shape of equation (15) is kept for the damping force calculation. The coefficients are obtained based on the ES-BGK solutions, which are $A = 10.39$, $B = 1.374$, $c = 3.100$, $d = 1.825$ and $e = 0.9660$.

The rational polynomial in equation (15) can be easily integrated and inverted. It is noted that under highly rarefied conditions, c_f tends to zero according to equation (15), which agrees with the asymptotic analysis of SFD under free-molecular conditions. In addition, it clearly shows that increasing the geometric aspect ratio, b/g, or decreasing the Knudsen number, $Kn^{(b)}$, will lead to an increase of the damping force, and vice versa.

In Veijola's model, the coefficients based on empirical approximations [19] are $A = 1.000$, $B = 9.683$, $c = 3.000$ and $d = e = 1.159$. Compared to the compact model based on rarefied flow simulations, it tends to over-estimate damping forces at large Kn numbers.

5.2. Statistical tests of the new model

Since the new model has its physical background as discussed above, the statistical tests that examine the goodness of fit of the model will not only show that the data and model fit well, but also verify the dependences of corresponding physic parameters, c_f, b/g and $Kn^{(b)}$.

Table 4. Statistical analysis of the ES-BGK-based compact model.

Property	Symbol	Value
Chi-square test	χ^2	1.058
Pearson's r^2	r^2	0.9980
Root mean square deviation	RMSD	7.809×10^{-4}
Mean absolute deviation	MAD	3.997×10^{-4}
Mean scaled absolute deviation	MSAD	6.085×10^{-3}
Root mean squared scaled deviation	RMSSD	3.281×10^{-2}
Mean deviation	MD	9.217×10^{-6}
Linear regression coefficients	β_0	1.315×10^{-4}
	β_1	0.989

Table 5. Microcantilever geometry and flow conditions [21].

Property	Symbol, unit	Nominal value
Cantilever length	L	$(300, 700, 800) \times 10^{-6}$ m
Cantilever width	b	20×10^{-6} m
Cantilever thickness	t_A	2.5×10^{-6} m
	t_B	2.25×10^{-6} m
Gap height	g_A	2.0×10^{-6} m
	g_B	6.3×10^{-6} m
Gas	(N_2, O_2)	Air
Cantilever	Si	Polysilicon
Cantilever density	ρ_s	2300 kg m^{-3}
Young's modulus	E	160 GPa
Temperature	T	295 K
Frequencies	f_{1A}	17 852 Hz
	f_{1B}	15 242 Hz

A summary of the statistical analysis can be found in table 4, which suggests that

(1) the model has a high fidelity (by the chi-squared test),
(2) the relative trend magnitudes are well captured (by the Pearson r^2) and
(3) the model predictions are close to observations (by for example the root mean squared deviation).

The test definitions can be found in most statistic textbooks, for example [20].

5.3. Applications to microcantilevers with low aspect ratios

5.3.1. Comparison with experimental data. In order to validate the new SFD model, predictions have been compared to microcantilever experiments by Ozdoganlar *et al* [21]. The ratios of cantilever widths to gap heights are 10.0 and 3.17. Three length cases are involved, which are 800, 700 and 300 μm. A summary of geometric and structural properties can be found in table 5.

As shown in figure 8, the predicted values of the quality factor agree very well with experimental data for pressure ranging from 5 Torr (0.0066 atm) to 200 Torr (0.26 atm) for different geometries and vibration modes. For pressure larger than 200 Torr, the differences between model predictions and experimental data are not surprising because the model coefficients are obtained from simulations where the flows are in transitional and free molecular regimes, i.e. $Kn > 0.1$. However, at very large Knudsen numbers, observations show that the model tends to give low predictions of the quality factor compared to experimental data.

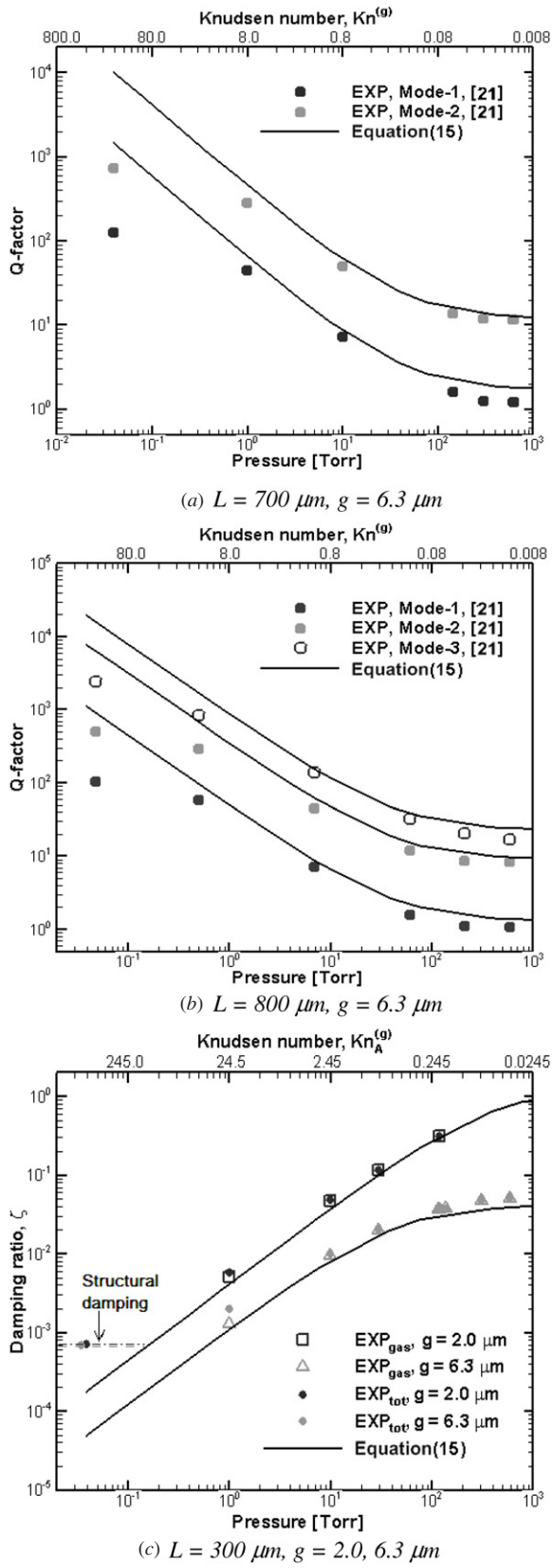

Figure 8. Comparisons of predictions by the ES-BGK-based correlation and experimental data in [21].

5.3.2. Boundary and structural damping effects. There are two important effects that need to be considered when comparing experimental damping measurements with gas damping predictions.

First, the boundary interference may affect the measured damping at extremely low pressures. For example, the experiment [21] was conducted for an array of microcantilevers, each separated by a distance of about 20 μm. The presence of neighboring cantilevers leads to an additional damping and, therefore, a lower quality factor. This boundary effect is expected to be significant when the gas mean-free-path is larger than the distance between cantilevers. For the cantilever array in [21], the air mean-free-path exceeds the inter-cantilever distance for pressures below 2 Torr (0.0026 atm).

Second, the measured quality factor includes both structural and gas damping. As noted in [21], the quality factors for the same microcantilever cross section at different gap heights converge to a constant value at low pressures. The structural damping is independent of the gas size and is negligible compared to the gas damping at moderate and atmospheric pressures. However, at low pressures, both structural and gas damping must be taken into account. A reader is referred to [7] for an excellent discussion and a method to extract the structural damping. As shown in figure 8(*c*), the total measured damping ratio, ζ_{tot}, at pressures $P_A < 0.1$ Torr (1.3×10^{-4} atm) is dominated by the structural damping. Here, we assume that the structural damping ratio equals to the value to which the experimental measurements for two different gap heights collapse at low pressures. When the structural damping is subtracted from the total measured value as shown in figure 8(*c*), the agreement between gas damping model and experimental data becomes very close even at low pressures.

6. Conclusions

In this work, we propose a compact model of squeeze-film damping based on ES-BGK calculations. The model gives a simple relationship between the gas damping coefficient (or quality factor) and two non-dimensional parameters: the ratio of the microcantilever width to the gap height, b/g, and the width-based Knudsen number, $Kn^{(b)}$. The model is based on a set of 50 ES-BGK simulations and a variety of tests for the goodness of fit have been performed. Model validation has been carried out by comparison with experimental data. When the structural damping is subtracted from the measured total damping force, good agreement is found between the model predictions and the experimental data.

Acknowledgments

The work is supported by NNSA Center for Prediction of Reliability, Integrity and Survivability of Microsystems at Purdue University under contract number DE-FC52-08NA28617. The authors would like to thank Professor Arvind Raman and Dr Jin-Woo Lee of Purdue University for extremely valuable discussion of the structural damping.

References

[1] Corman T, Enoksson P and Stemme G 1997 Gas damping of electrostatically excited resonators *Sensors Actuators* A **61** 249–55
[2] Zook J *et al* 1992 Characteristics of polysilicon resonant microbeams *Sensors Actuators* A **35** 51–9
[3] Chang K M, Lee S C and Li S H 2002 Squeeze film damping effect on a MEMS torsion mirror *J. Micromech. Microeng.* **12** 556
[4] Pan F *et al* 1998 Squeeze film damping effect on the dynamic response of a MEMS torsion mirror *J. Micromech. Microeng.* **8** 200–8
[5] Veijola T *et al* 1999 Dynamic simulation model for a vibrating fluid density sensor *Sensors Actuators* A **76** 213–24
[6] Spletzer M *et al* 2006 Ultrasensitive mass sensing using mode localization in coupled microcantilevers *Appl. Phys. Lett.* **88** 254102–3
[7] Sumali H 2007 Squeeze-film damping in the free molecular regime: model validation and measurement on a MEMS *J. Micromech. Microeng.* **17** 2231–40
[8] Binnig G, Quate C F and Gerber C 1986 Atomic force microscope *Phys. Rev. Lett.* **56** 930
[9] Bao M and Yang H 2007 Squeeze film air damping in MEMS *Sensors Actuators* A **136** 3–27
[10] Bird G A 1994 *Molecular Gas Dynamics and the Direct Simulation of Gas Flows* (New York: Oxford University Press)
[11] Meirovitch L 2000 *Principles and Techniques of Vibrations* 2nd edn (Englewood Cliffs, NJ: Prentice-Hall)
[12] Veijola T 2004 Compact models for squeezed-film dampers with inertial and rarefied gas effects *J. Micromech. Microeng.* **14** 1109–18
[13] Gallis M A and Torczynski J R 2004 An improved Reynolds-equation model for gas damping of microbeam motion *J. Microelectromech. Syst.* **13** 653–9
[14] Karniadakis G, Beskok A and Aluru N 2005 *Microflows and Nanoflows: Fundamentals and Simulation (Interdisciplinary Applied Mathematics)* (Berlin: Springer)
[15] Mieussens L and Struchtrup H 2004 Numerical comparison of Bhatnagar–Gross–Krook models with proper Prandtl number *Phys. Fluids* **16** 2797–813
[16] Shizgal B 1981 A Gaussian quadrature procedure for use in the solution of the Boltzmann equation and related problems *J. Comput. Phys.* **41** 309–28
[17] Guo X *et al* 2008 Gas-phonon interaction model for subcontinuum thermal transport simulations *Proc. 26th RGD (Kyoto, Japan, 2008)*
[18] Sandia. CINT webpage, cited; available at http://cint.lanl.gov/
[19] Veijola T *et al* 1995 Equivalent-circuit model of the squeezed gas film in a silicon accelerometer *Sensors Actuators* A **48** 239–48
[20] Devore J L *Probability & Statistics for Engineering & the Sciences* (Belmont, CA: Brooks Cole)
[21] Ozdoganlar O B, Hanshce B D and Carne T G 2005 Experimental modal analysis for micro-electro-mechanical systems *Exp. Mech.* **45** 498–506